Full length article

Electronic-structure tuning of honeycomb layered oxide cathodes for superior performance

Lei Xiao [a,1], Zhengping Ding [b,1], Qun Huang [a,1], Cheng Chen [a], Yiming Feng [a], Chaoping Liang [a], Peng Gao [b,*], Weifeng Wei [a,*]

[a] State Key Laboratory of Powder Metallurgy, Central South University, Changsha, Hunan 410083, People's Republic of China
[b] International Center for Quantum Materials, and Electron Microscopy Laboratory, School of Physics, Peking University, Beijing 100871, People's Republic of China

ARTICLE INFO

ABSTRACT

Recently honeycomb-ordered $Na_3M_2XO_6$ (M = Ni, Cu, Co; X = Sb, Bi etc.) layered oxide cathode materials have attracted significant interest because of their excellent voltage platform and high energy density. Despite their excellent prospects, they still suffer from insufficient rate capability and poor structure stability. Herein, we find that the specific capacity, electronic conductivity and structural stability of honeycomb-ordered $Na_3Ni_2SbO_6$ cathode material can be well promoted through partial Ru substitution. By combining the experimental analyses and theoretical calculations, we reveal that the partial substitution of Sb(V) with low valence Ru(IV) generated a strong Ru-O covalency reduces the bandgap, leading to a decreased redox potential and enhanced electrochemical kinetics. Meanwhile, the formed honeycomb $RuNi_6$-ring superstructure with structural distortion can adapt large strain fluctuation during cycling and eventually enhance the electrochemical cyclability. Such a proposed strategy provides valuable insights into further developments of the high-performance honeycomb layered oxides cathodes.

1. Introduction

The severe scarcity of lithium resources has led to the growing concerns about the application potentials of lithium-ion batteries (LIBs) in large-scale energy storage [1–3]. Among many other energy storage systems, sodium-ion batteries (SIBs) are gaining higher possibility in sustainability and affordability given the rich resources and low cost [4–7]. Since the early 1980s, great efforts have been devoted to the cathode materials for SIBs, and among them, layered transition metal oxides with a general formula of Na_xMO_2 (x≤1, M = Fe, Co, Ni, Mn, Cr, V, and etc.) have been extensively discussed used in sustainable energy storage application model [8–10]. According to Delmas et al., layered transition metal oxides can be generally grouped into P2- and O3-types, where Na^+ occupy the prismatic and octahedral sites, respectively [11,12]. The O3-type oxides can host a higher Na content than the P2 oxides, making it possible to obtain a higher reversible specific capacity, especially in sodium full-cells [13–16]. Among these O3-type compounds, honeycomb-ordered $Na_3M_2XO_6$ materials (M = Ni, Cu, Co; X = Sb, Bi) have attracted great attention due to their rela-

tively high voltage profile (average voltage > 3.3V) and high reversible capacity within the voltage range from 2 to 4V [17,18]. However, they still suffer from poor cycle stability and insufficient rate performance owing to the irreversible O3-P3-O1 phase transformation and structural collapse during Na^+ insertion/extraction process, impeding their practical application in SIBs [19–21]. To address these issues, heterogeneous ion-substitution using other electrochemically inactive cations such as Mg^{2+}, Zn^{2+}, has been employed to achieve good cycling stability [22,23]. However, due to the incorporation of inactive species, chemical substitution generally brings about capacity loss. Thus far, it remains challenging to obtain simultaneous improvements in specific capacity, rate capability and cycling stability.

From this perspective, herein, for the first time we present an electronic-structure modulation strategy through partial substitution of Sb with Ru to concurrently increase the reversible capacity, cycling capability and rate performance of the honeycomb-ordered $Na_3Ni_2SbO_6$ compound. The formation of $RuNi_6$-ring superstructure induced by the strong covalence of active Ru with oxygen facilitates the generation of the electronic holes for the O-2p band and lowers the band gap of the $Na_3Ni_2Sb_{0.8}Ru_{0.2}O_6$ compound, resulting in higher ionic and electronic conductivities and effective suppression of the structure collapse occurred in a deep state of charge. These results demonstrate the relationship between the

modulation of honeycomb superstructure and enhanced the electrochemical performance in O3 layered oxides, providing useful clues for designing high-performing cathode materials of SIBs.

2. Experimental section

2.1. Synthesis of $Na_3Ni_2Sb_{1-x}Ru_xO_6$

A simple solution combustion method combined with stepwise high-temperature treatment were employed to synthesize the $Na_3Ni_2Sb_{1-x}Ru_xO_6$ (x = 0, 0.1, 0.2 and 0.3). Specifically, stoichiometric amounts of $NaNO_3$, $Ni(CH_3COO)_2$, $Sb(CH_3COO)_3$, RuO_2 and glucose were uniformly dissolved/dispersed in deionized water. The mixture was heated at 80°C in a water bath to evaporate the extra water until it turned into gel. Then, the gel was transferred to a crucible and heated to 250°C then spontaneously combustion reaction occurred. The obtained precursor was ground by using an agate mortar and collected it in a corundum boat. Finally, the precursor was annealed at 800°C for 15h in a muffle furnace under air atmosphere to obtain the target product. All samples were transferred into glove box with argon-filled atmosphere for storage.

2.2. Materials characterization

Inductively coupled plasma-atomic emission spectrometry (ICP-AES) was conducted to determine the chemical composition of the samples. The crystallographic structure of the samples was investigated using X-ray diffraction (XRD) with a Cu-Kα radiation in the range of 10–80° (Bruker Advance D8 powder diffractometer, 0.02° 2θ per step and 2 s duration). Rietveld refinement of the XRD patterns was carried out by using GSAS+EXPGUI software [2]. Field emission scanning electron microscopy (SEM, FEG250, FEI QUANTA) was used to observe the morphology of the samples. An ESCALAB 250Xi X-ray photoelectron spectrometer (XPS) was applied to determine the chemical state of the elements. All XPS spectra were calibrated using the C 1s peak with a binding energy of 284.8 eV. Background subtraction and curve fitting were fulfilled using XPSPEAK Version 4.0 software. The atomic-resolution high angle annular dark field scanning transmission electron microscopy (HAADF-STEM) and electron energy loss spectroscopy (EELS) were conducted on an aberration-corrected FEI (Titan Cubed Themis G2) equipped with an X-FEG gun at 300 kV, accompanied by the ~50 pA beam current. The convergence semi-angle was 30 mrad and the collection semi-angle snap range was from 80 to 379 mrad. The STEM-EDS mapping were acquired on a Bruker Super-X EDS four-detector with a beam current of ~100 pA and counts ranging from 1k cps to 3k cps for ~15 min. The EELS data was collected by Gatan Enfinium system with the collection semi-angle of 5.9 mrad, the convergence semi-angle of 25 mrad and a dispersion of 0.25 eV/ch.

2.3. Electrochemical characterizations

All the cathode materials were mixed with acetylene black and polyvinylidene fluoride (PVDF) binder at the weight ratio of 8:1:1 and then dissolved completely in N-methyl-2-pyrrolidone (NMP). After stirring for 1h, the obtained slurry was homogeneously pasted onto Al foil and dried at 110°C for 12 h in a vacuum oven. The coated foil was cut into circular pieces with a diameter of 12 mm. A cathode electrode piece, a separator (glass fiber) and a metallic sodium anode were assembled into a coin-type half-cell (CR 2016) in an Ar-filled glove box (MBraun, Germany). The electrolyte solution was prepared through dissolving 1 M $NaPF_6$ in ethylene carbonate (EC)/dimethyl carbonate (DEC) (1:1, v/v) with 3 vol% fluoroethylene carbonate (FEC). The cycle and rate tests were performed on Land cell test system at room temperature, in a voltage window of 2V-4V (vs. Na^+/Na). Electrochemical impedance spectroscopy (EIS) was tested on an electrochemical workstation (PARSTAT 4000 A Potentiostat/Galvanostat, Princeton Applied Research) and recorded at a frequency of 0.1 Hz–100 kHz with an AC amplitude of 5 mV at room temperature.

2.4. Na^+ diffusion coefficients

The Na^+ diffusion coefficient (D_{Na+}) is calculated based on the following equation:

$$D_{Na+} = \frac{R^2T^2}{2A^2n^4F^4C^2\sigma^2}$$

Where R is the molar gas constant (8.314 J•K•mol^{-1}), T is the thermodynamic temperature (303K), A is the area of cathode electrode (1.1309 cm^2), n is the number of electrons every molecule participating in the redox reaction (1), F is the Faraday constant (96500 C mol^{-1}), C is the Na^+ concentration in cathode material (0.05) and σ is Warburg coefficient (Table S7).

2.5. First-principle calculations

First-principle calculations based on density functional theory (DFT) were performed using the Vienna Ab-initio Simulation Package (VASP) package. The generalized gradient approximation (GGA) with the Perdew−Burke−Ernzerhof (PBE) functional was used to describe the electronic exchange and correlation effects. Uniform G-centered k-points meshes with a resolution of $2\pi*0.03$ Å^{-1} and Methfessel-Paxton electronic smearing were adopted for the integration in the Brillouin zone for geometric optimization. The simulation was run with a cutoff energy of 520 eV throughout the computations. These settings ensure the convergence of the total energies to within 1 meV per atom. Structure relaxation proceeded until all forces on atoms were less than 1 meV Å^{-1} and the total stress tensor was within 0.01 GPa of the target value. To describe the on-site Coulomb interaction, the DFT +U approach was used to calculate all the elementary reaction steps, and the U term of Ni-3d and Ru-4d is 6.8 and 4.0 eV, respectively. The layered structure of $Na_3Ni_2SbO_6$ was adopted as initial structure to build the Ru doped compounds. In order to get the $Na_3Ni_2Sb_{0.8}Ru_{0.2}O_6$ structure model, a 6 × 1 × 1 supercell with the chemical formula of $Na_{18}Ni_{12}Sb_6O_{36}$ was built. The coordination environment of Ni or Sb atoms is the same, so the Ni or Sb atom can be randomly replaced by Ru to get the $Na_{18}Ni_{12}Sb_5Ru_1O_{36}$ or $Na_{18}Ni_{11}Sb_6Ru_1O_{36}$ supercells.

3. Results and discussion

3.1. Crystal structure analysis

The elemental composition of the $Na_3Ni_2Sb_{1-x}Ru_xO_6$ compounds determined by Inductively coupled plasma-atomic emission spectrometry (ICP-AES) (Table S1), indicates well consistent along with the designed stoichiometry. Scanning electron microscopy (SEM) images of the as-prepared samples (Fig. S1) show that all $Na_3Ni_2Sb_{1-x}Ru_xO_6$ samples display irregular flaky morphology with particle size ranging from 0.5 to 1.5μm. As shown in Figs. S2 and S3, high angle annular dark field-scanning transmission electron microscopy (HAADF-STEM) images and the corresponding EDS mappings demonstrate the homogeneous distribution of Na, Ni, O, Sb and Ru elements in the layered oxides. As illustrated in Fig. 1a, the X-ray diffraction (XRD) peaks of all the samples can be fully indexed to a monoclinic phase with space group $C2/m$, without any impurities after Ru substitution. The weak diffraction
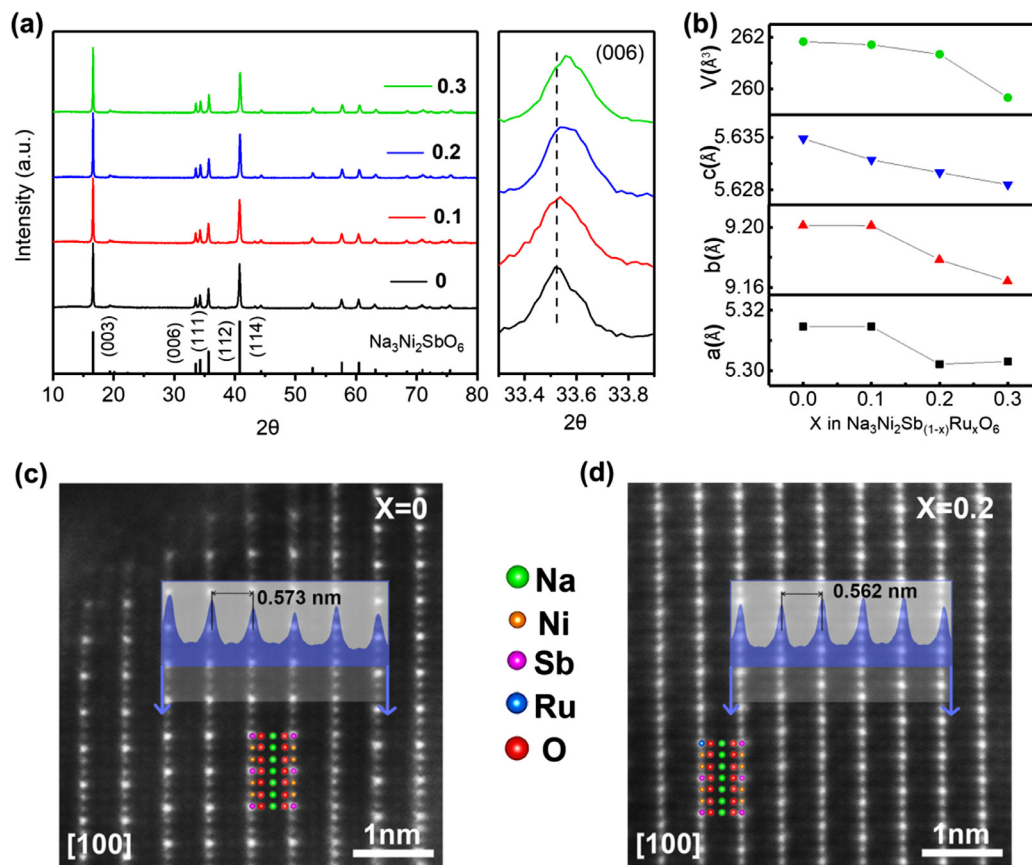
Fig. 1. (a) Powder XRD patterns of the $Na_3Ni_2Sb_{1-x}Ru_xO_6$ samples. (b) Refined lattice parameters of the $Na_3Ni_2Sb_{1-x}Ru_xO_6$ samples. HAADF-STEM images and corresponding Z-contrast profiles with measured spacing of (c) $Na_3Ni_2SbO_6$ and (d) $Na_3Ni_2Sb_{0.8}Ru_{0.2}O_6$ observed along [100] zone axis.

peaks located at 18-32° are attributed to the superstructure reflections of honeycomb-ordered Ni/Sb arrangement within *ab*-plane [21]. The Rietveld refined XRD patterns and the fitting results are presented in Figs. S4 and 1b and Tables S2–S5. It is evident that the lattice and volume parameters decrease steadily with the increase of Ru content, which is in good agreement with the shifting of the (006) peak in Fig. 1a. Further, as shown in the atomic-resolution HAADF-STEM image along [100] direction (Fig. 1c and 1d), the spacing of TM layers become smaller after Ru doping, suggesting shrinkage of crystal volume, which is consistent well with XRD analysis results. The slight decreasing of the unit cell lattice could be ascribed to the different bonding strength between Ru-O and Sb-O bonds, resulting in the shrinkage of the RuO_6 octahedron than the SbO_6 octahedron in Ni_2SbO_6 layers. Such a difference will be discussed later in detail.

To figure out the atomic-scale structure variation induced by Ru substitution, HAADF-STEM images along the [100] zone axis taken from the $Na_3Ni_2SbO_6$ and $Na_3Ni_2Sb_{0.8}Ru_{0.2}O_6$ samples are illustrated in Fig. S5a and S5b. Considering that the HAADF image contrast is roughly proportional to Z1.7 (Z represents the atomic number) [2], the brighter and darker spots correspond to Sb and Ni atoms, respectively, showing the Sb-Ni-Ni-Sb ordered arrangement in the Ni_2SbO_6 layer. However, different atomic arrays against the Sb-Ni-Ni-Sb ordered arrangement is also found in pristine $Na_3Ni_2SbO_6$ sample (red frame in Figure S5a), indicating an imperfect Ni/Sb honeycomb-ordered arrangement in *ab*-plane. In contrast, $Na_3Ni_2Sb_{0.8}Ru_{0.2}O_6$ shows a highly-ordered honeycomb arrangement, suggesting that Ru substitution can effectively improve the in-plane honeycomb ordering. Besides, the contrasts between the bright and dark spots in the Ni_2SbO_6 layer of the two samples are rather different. To quantify this difference,

the Ni_2SbO_6 layer contrast intensity profiles of the two different samples are presented in Fig. S5c, which are taken from the yellow rectangle area in Fig. S5a and S5b. It is evident that the difference between the high peaks and low peaks in the $Na_3Ni_2SbO_6$ cathode material is larger than that in the $Na_3Ni_2Sb_{0.8}Ru_{0.2}O_6$ sample. In addition, the HAADF-STEM images of the two samples projected along [010] and [001] zone axis are presented in Fig. S6. As it has been reported in our previous study, the rotation of layers induce out-of-plane stacking disorder, making the Sb/Ni superstructure cannot be observed from the [010] and [001] zone axis [24]. Since the atomic number of Ru (44) is smaller than that of Sb (51) but larger than that of Ni (28), hence it is hard to determine whether Ru substitutes the Sb site or Ni site based merely on the HAADF-STEM results.

In this regard, first-principles calculations were performed to confirm the substitution site of Ru^{4+} ions [25,26]. By calculating the formation energy (H_f) of $Na_3Ni_2Sb_{0.8}Ru_{0.2}O_6$ compound with different Ru^{4+} substitution sites, the thermodynamic stability of different Ru occupancies can be determined. The formulas for calculating the H_f of Ru substituted at Sb and Ni sites are as follows,

$$H_f(Na_{18}Ni_{12}Sb_5RuO_{36})$$
$$= E(Na_{18}Ni_{12}Sb_5RuO_{36}) + \frac{1}{2}E(Sb_2O_5)$$
$$- E(Na_{18}Ni_{12}Sb_6O_{36}) - \frac{1}{2}E(RuO_2) - E(O_2) \quad (1)$$

$$H_f(Na_{18}Ni_{11}Sb_6RuO_{36}) = E(Na_{18}Ni_{11}Sb_6RuO_{36}) + E(NiO_2)$$
$$- E(Na_{18}Ni_{12}Sb_6O_{36}) - E(RuO_2) \quad (2)$$

Fig. 2. (a-b) EELS spectra of the $Na_3Ni_2SbO_6$ and $Na_3Ni_2Sb_{0.8}Ru_{0.2}O_6$ samples. (c) The corresponding total and partial density of states (DOSs) of TM and O ions. (d) The relaxed crystal structures of the $Na_3Ni_2SbO_6$ and $Na_{3Ni2Sb0.8Ru0.2O6}$ viewed from the [001] zone axis. (e) The calculated charge density and charge density difference (CDD) for Sb and Ru maps of SbNi6-ring(left) and RuNi6-ring (right). The CDD maps are calculated by the formula: $\Delta\rho=\rho$(total)- ρ(total-Ru/Sb)- ρ(Ru/Sb). The yellow and blue part in charge density difference images represent the gain and loss of electrons, respectively.

where $E(Na_{18}Ni_{12}Sb_5RuO_{36})$ or $E(Na_{18}Ni_{11}Sb_6RuO_{36})$ is the total formation energy of substituted compound, $E(Na_{18}Ni_{12}Sb_6O_{36})$ is the total formation energy of pristine compound, and $E(RuO_2)$, $E(Sb_2O_5)$, $E(NiO_2)$ and $E(O_2)$ are the formation energies of RuO_2, Sb_2O_5, NiO_2 and O_2 gas, respectively. The calculated formation energy of all the compounds mentioned in Eqs. (1) and (2) are listed in Table S6. The lower value of $H_f(Na_{18}Ni_{12}Sb_5RuO_{36})$ than $H_f(Na_{18}Ni_{11}Sb_6RuO_{36})$ suggests a preferential occupancy of Ru in the Sb site, probably due to the similarities in ionic radius and valence state between Ru and Sb without affecting its in-plane honeycomb ordering by the Ni_6-rings [27–29].

3.2. Electronic structure variations

To appreciate the electronic structure changes induced by Ru substitution, complementary electron energy loss spectroscopy (EELS) (Fig. 2a and 2b) and X-ray photoelectron spectroscopy (XPS) analyses (Figure S7) were performed on pristine and Ru-substituted materials. Ru substitution brings about nearly no changes to the EELS Ni-$L_{2,3}$ edges and the Ni 2p XPS spectra. In contrast, as for the Sb ions, a small shift to lower energy values for the Sb 3d XPS spectra can be observed in Fig. S7c, indicating a very slight decrease in Sb-O binding energy (Sb $3d_{3/2}$ peak shift from 539.04 eV to 538.89 eV). As shown in Fig. 2b, the O K-edge pre-peak at 530 eV accounts for the hybridization between the O-2p band and the transition metal 3d band, which can reflect the valence state of transition metal [30–32]. By comparison, the pre-peak position do not change after Ru-doped, suggesting that the valence state of Sb and Ni have no change. Moreover, the second main peak for O K-edge accounts for the transitions to O-2p states hybridized with the more-delocalized transition-metal 4s and 4p states, reflecting the intrashell multiple scattering within the first oxygen coordination shell which is related to the first-neighbor O-O distance in compound [31–33]. The main peak for O K-edge shift to a lower energy after Ru substitution, implying a little higher O-2p valence state and oxygen vacancy formation. That is mainly attribute to partial Sb substituted by Ru, which has a stronger interaction with the neighboring O and weaken the Sb-O bonding through the surrounded Ni_6-ring superstructure. Thus, the substitution of high valent Sb^{5+} with low valent Ru^{4+} makes rather marginal impacts on the chemical coordination environments of Ni and Sb cations, which can be related to the honeycomb-ordered Ni_6-ring superstructure that weakens the effect on chemical environments [27].

To rationalize this idea, density-functional-theory (DFT) calculations were conducted to obtain the total and partial density of states (DOSs) of Ni, Sb, Ru and O ions, as illustrated in Fig. 2c. As expected in the relaxed honeycomb-layered structure, each SbO_6
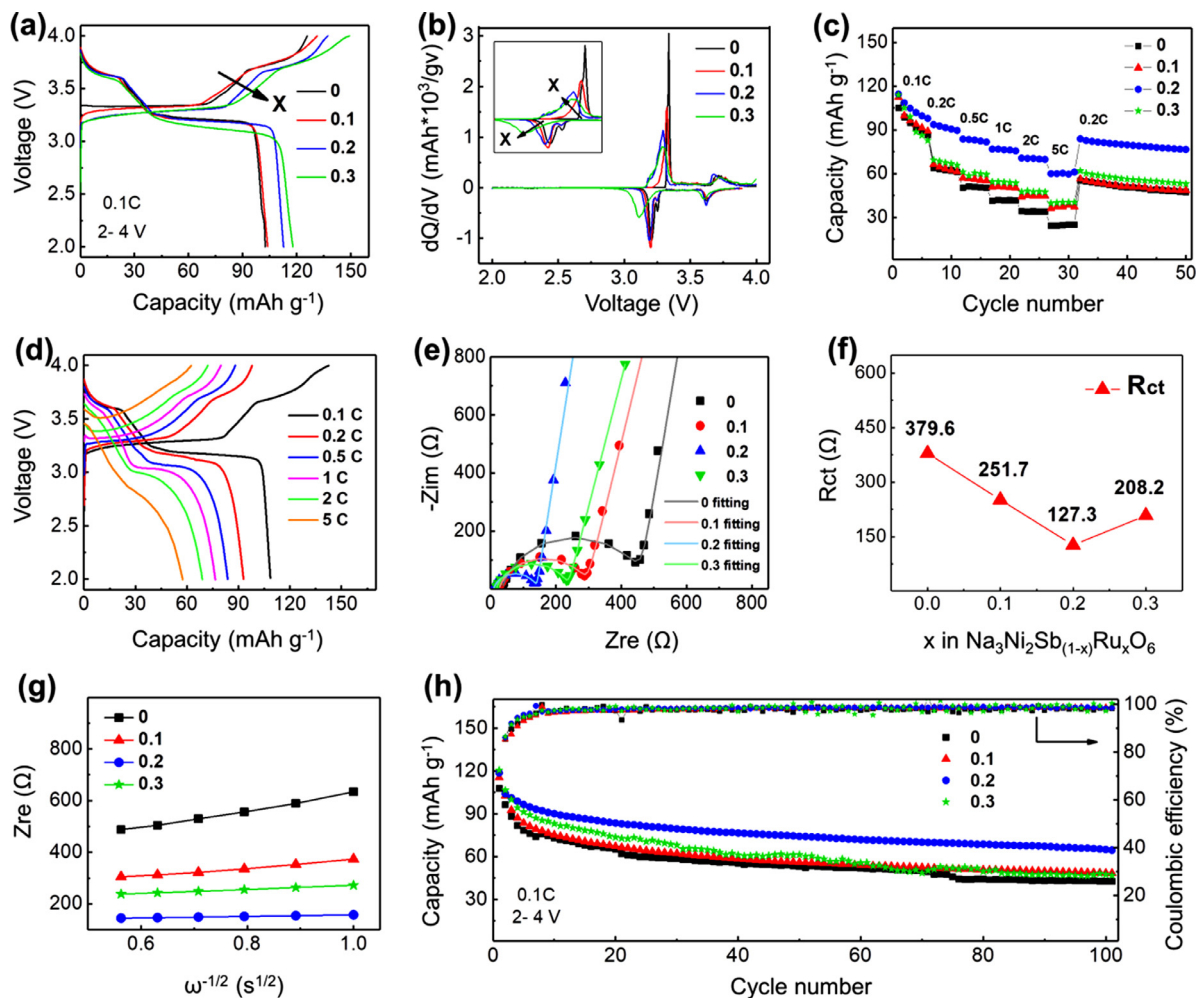
Fig. 3. Electrochemical performance of the $Na_3Ni_2Sb_{1-x}Ru_xO_6$ cathodes including (a) First galvanostatic charge/discharge curves at a rate of 0.1C, (b) Corresponding dQ/dV curves, (c) Rate performance of all samples at various rates and (d) Charge/discharge curves of $Na_3Ni_2Sb_{0.8}Ru_{0.2}O_6$ sample at different rates. (e) Nyquist plots of the $Na_3Ni_2Sb_{1-x}Ru_xO_6$ samples and the simulated curves fitted by equivalent circuit. (f) The Rct of $Na_3Ni_2Sb_{1-x}Ru_xO_6$ samples after equivalent circuit fitting. (g) Zre vs. $\omega^{-1/2}$ diagram with linear fitting results of all samples. (h) Cycling performance of $Na_3Ni_2Sb_{1-x}Ru_xO_6$ samples at 0.1C rate.

octahedron (purple) surrounded by six NiO_6 octahedra (orange) to form the TM layer in $Na_3Ni_2SbO_6$ structure, where one fifth of the Sb cations are occupied by Ru cations in $Na_3Ni_2Sb_{0.8}Ru_{0.2}O_6$ structure (Fig. 2d). It is evident that the incorporation of Ru cations makes nearly no impacts on the DOS profiles of Ni and Sb, which is well consistent with the experimental EELS and XPS results. Nevertheless, the 4d empty orbitals introduced by Ru^{4+} and the strong covalency of active Ru cations with oxygen that facilitates the generation of the electronic holes for the O-2p band, which can lower the band gap of the compound by about 0.7 eV. This indicates that the $Na_3Ni_2Sb_{0.8}Ru_{0.2}O_6$ structure, which possesses active Ru^{4+} cations and exhibits a lower band gap, would display a decreased redox potential and enhanced electrochemical kinetics when compared with the $Na_3Ni_2SbO_6$ structure. In addition, the calculated charge density and charge density difference (CDD) in Fig. 2e compares the electronic structure of $SbNi_6$-ring and $RuNi_6$-ring. The Ni_6-ring superstructure with a Sb center, the charge density around the Sb is evenly distributed and exhibits a polygon-like shape. In contrast, as a Ru located at the Ni_6-ring center, the charge distribution around the Ru center shows a strong tendency concentrated along the neighboring O, suggesting that the strength of Ru-O bond is higher than that of the Sb-O bond and the electronic conductivity of $RuNi_6$-ring superstructure is better than the $SbNi6$-ring superstructure [27,34]. All these DFT calculation results including

DOS and CDD suggest that partial substitution of Sb by Ru may enhance the electrochemical kinetics and structural stability of the $Na_3Ni_2Sb_{0.8}Ru_{0.2}O_6$ layered cathode material.

3.3. Electrochemical performance

The electrochemical tests of $Na_3Ni_2Sb_{1-x}Ru_xO_6$ (x = 0, 0.1, 0.2, and 0.3) were performed using Na half-cells in a voltage range of 2.0−4.0 V (Fig. 3). The initial charge-discharge profiles and corresponding derivative capacity–potential (dQ/dV) plots of all cathodes at 0.1C (1C=200 mA g^{-1}) are displayed in Fig. 3a and 3b. The pristine $Na_3Ni_2SbO_6$ (x=0) exhibits two main discharge plateaus at about 3.3 V and 3.65 V with a few of small shoulder peaks neighboring them, indicating multiple intermediate phase transitions during charge/discharge process. With the stepwise increase of Ru content (x increased from 0.1 to 0.3), the discharge plateau at about 3.3V gradually shifts to a lower voltage and merged with the neighboring peaks, which suggests that intermediate phase transitions are effectively suppressed by Ru substitution. Changes in charge-discharge curve shapes are mainly due to the electrochemical activation of $Ru^{4+}+^{/5+}+$ redox couple which possesses a long platform near 2.6V and the formation of Ru–Ru dimers [35-37]. The initial discharge capacity of the $Na_3Ni_2Sb_{1-x}Ru_xO_6$ cathodes increases with the Ru content, exhibiting 102.5, 103.9, 112.7 and
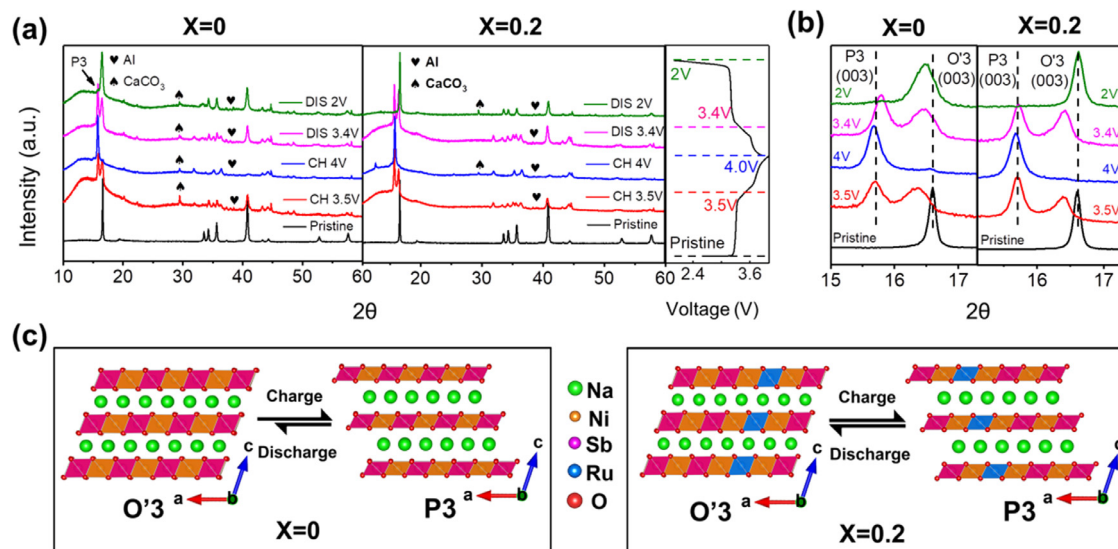
Fig. 4. (a) Ex situ XRD patterns of $Na_3Ni_2SbO_6$ and $Na_3Ni_2Sb_{0.8}Ru_{0.2}O_6$ cycled to different states of charge at the voltage points of 3.5V and 4V, and discharge at 3.4V and 2V. (b) The enlarged ex situ XRD patterns of $Na_3Ni_2SbO_6$ and $Na_3Ni_2Sb_{0.8}Ru_{0.2}O_6$ in the region of 15°−17.3°. (c) Schematic illustration of structural variations in $Na_3Ni_2SbO_6$ (left) and $Na_3Ni_2Sb_{0.8}Ru_{0.2}O_6$ (right) during charge/discharge process.

117.8 mAh g^{-1}, respectively. Considering that Ru substitution can effectively improves the electronic and ionic conductivity of the doped-materials, the enhanced electrochemical kinetics allow the extraction and reinsertion of more Na ions within the same voltage range of 2.0-4.0 V vs. Na+/Na, explaining the extra reversible capacities achieved in the Ru-doped materials. Fig. 3c compares the rate capability of all the cathodes in the voltage range of 2.0-4V versus Na+/Na. At all C-rates, the $Na_3Ni_2Sb_{1-x}Ru_xO_6$ sample with x=0.2 shows the optimized rate performance, delivering discharge capacities of 114.6, 93.7, 83.8, 76.9, 70.7 and 60 mAh g^{-1} at current rates of 0.1C, 0.2C, 0.5C, 1C, 2C, and 5C, respectively (Fig. 3d). The enhanced rate performance of cathode materials may attribute to the enhanced electronic conductivity and Na+ transport kinetics especially at high rates.

To understand the enhanced electrochemical kinetics, electrochemical impedance spectroscopy (EIS) analysis of $Na_3Ni_2Sb_{1-x}Ru_xO_6$ cathodes was conducted and the results are shown in Fig. 3e–3g [38–42]. The Nyquist plots of all samples exhibit similar profiles with a semicircle in the high frequency and a sloping line in the low frequency, corresponding to the charge transfer resistance (R_{ct}) and the Warburg impedance (W_o), respectively. In comparison, the $Na_3Ni_2Sb_{0.8}Ru_{0.2}O_6$ cathode displays the smallest R_{ct} and a fast charge transfer kinetics, which is consistent with the lower band gap after Ru substitution that results in improved electronic conductivity (Fig. 2c). In addition, the Na+ diffusion coefficients (D_{Na+}) of all samples were also calculated. By comparing the calculated value of D_{Na+}, x=0.2 sample demonstrates the highest diffusion coefficients, inferring that Ru substitution greatly enhance the Na+ diffusion kinetics by expanding the d-spacing between Na+ diffusion layers (Tables S7 and S8) [43–46]. Note that the further increase of Ru content to 0.3 cause the reduction of d-spacing in the lattice, deteriorating the rate capability of the $Na_3Ni_2Sb_{0.7}Ru_{0.3}O_6$ electrode.

The effect of Ru substitution on cycling performance is demonstrated in Fig. 3h. It is worth noting that $Na_3Ni_2Sb_{0.8}Ru_{0.2}O_6$ cathode displays the optimal cycling stability. When cycled at 0.1C, a capacity retention of pristine $Na_3Ni_2SbO_6$ cathode is only 39.5% (44.1 mAh•g^{-1}) after 100 cycles, while the $Na_3Ni_2Sb_{0.8}Ru_{0.2}O_6$ displays a reversible capacity of 64.5 mAh g^{-1} with a capacity retention of 55% (Fig. S8). Even cycled for 200 times at 1C rate, $Na_3Ni_2Sb_{0.8}Ru_{0.2}O_6$ still possess the highest reversible capacity of

54 mAh g^{-1} with a capacity retention of 48.5% (Fig. S9). It is worth noting that, however, the cycling stability of Na3Ni2Sb1-xRuxO6 cathodes also declines when Ru content reaches x = 0.3, which can be ascribed to the fact that excessive amount of active Ru species might weaken the structure stability by interrupting Ni/Sb ordering [19,20], as shown in Figure S10. The above results indicate that an appropriate amount of Ru substitution can apparently improve the cycling stability and rate performance of $Na_3Ni_2SbO_6$ cathode through enhancing electrochemical kinetics and structure stability.

3.4. Phase transformation and structural evolution

To appreciate the origin of the enhancement in structure stability, phase transition and structural evolution during the first cycle were characterized via ex situ XRD. As shown in Fig. 4a, ex situ XRD patterns of the $Na_3Ni_2SbO_6$ and $Na_3Ni_2Sb_{0.8}Ru_{0.2}O_6$ cathodes were collected at different states of charge (SOC). For both materials, the O'3-P3-O'3 phase transformation process occurs upon Na+ desertion/insertion. Different from some previous reports on $Na_3Ni_2SbO_6$, no O1 phase can be observed at 4V charged state, which is due to the different degree of ordering in $Na_3Ni_2SbO_6$ [19,21,22,23]. The diffraction peaks of calcium carbonate impurity is brought by the plasticine, which was used to fix the electrode piece on the XRD sample stage. Fig. 4b compares the magnified ex situ XRD diffraction patterns of the NaNa3Ni2SbO6 and $Na_3Ni_2Sb_{0.8}Ru_{0.2}O_6$ samples in the region of 15°−17.3° to explicitly show the effect of Ru substitution on structural evolution. In addition to a trace amount of residual P3 phase, the peak broadening and shifting to a lower angle are evident in O'3-(003) diffraction peak for the discharged $Na_3Ni_2SbO_6$ cathode, implying less insertion of Na+ and poor structure reversibility of pristine $Na_3Ni_2SbO_6$, as schematically illustrated in Fig. 4c (left). In contrast, the $Na_3Ni_2Sb_{0.8}Ru_{0.2}O_6$ sample remains well crystallinity and no peak shift of O'3-(003) diffraction peak can be observed after the initial cycle, demonstrating effective improvements on phase transition reversibility, Na+ storage capability and structural stability (right panel in Fig. 4c). The XRD patterns of these samples after 100 cycles at 0.1C rate are depicted in Fig. S11 to further confirm the positive effect of Ru substitution on structural reversibility, where the $Na_3Ni_2Sb_{0.8}Ru_{0.2}O_6$ electrode maintains pure O'3 struc-
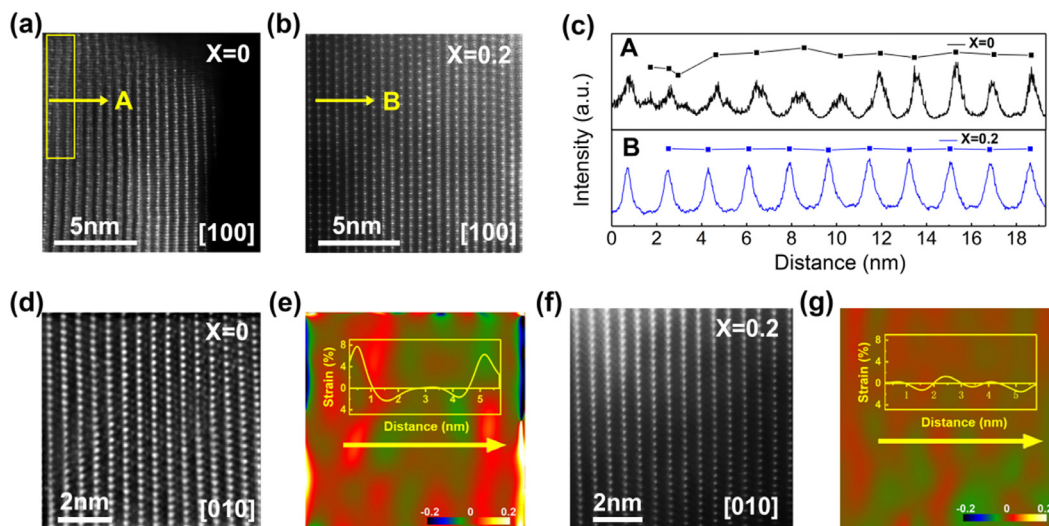
Fig. 5. Atomic resolution HAADF-STEM images of (a) $Na_3Ni_2SbO_6$ and (b) $Na_3Ni_2Sb_{0.8}Ru_{0.2}O_6$ in [100] zone axis at 4V charged state. (c) The corresponding atomic contrast and slab distance of $Na_3Ni_2SbO_6$ (bottom) and $Na_3Ni_2Sb_{0.8}Ru_{0.2}O_6$ (top). HAADF-STEM images of (d) $Na_3Ni_2SbO_6$ and (f) $Na_3Ni_2Sb_{0.8}Ru_{0.2}O_6$ in [010] zone axis at 4V charged state. Corresponding geometric phase analysis (GPA) patterns of (e) $Na_3Ni_2SbO_6$ and (g) $Na_3Ni_2Sb_{0.8}Ru_{0.2}O_6$ materials.

ture while the $Na_3Ni_2SbO_6$ sample still possesses some residual P3 phase.

To understand the enhancement in structural integrity induced by Ru substitution in atomic scale, HAADF-STEM imaging of the charged $Na_3Ni_2SbO_6$ and $Na_3Ni_2Sb_{0.8}Ru_{0.2}O_6$ materials was performed and compared in Fig. 5. Apparently, as shown in Fig. 5a and 5b, the lattice of the charged $Na_3Ni_2SbO_6$ material was severely distorted, demonstrating misplaced TM layers and cation mixing (yellow frame). Compared with the pristine material, the $Na_3Ni_2Sb_{0.8}Ru_{0.2}O_6$ exhibits a consistent interlayer distance and perfect atomic arrangement, indicating a well preserved in-plane honeycomb ordering even at deep Na^+ extracted state (Fig. 5c). On the other hand, atomic-scale simulated geometric phase analysis (GPA) was also conducted to study the internal strain and structure distortion (Fig. 5d–5g) [47]. Evidently, the pristine material display large strain distribution especially in the distorted area, while a relatively smaller and uniform internal strain distribution is observed in the Ru-substituted material. In other words, due to the enhanced stability of $Ni_2Sb(Ru)O_6$ layer induced by the strong Ru-O interaction, the structural stability of the cathode material is significantly improved and the lattice distortion is well suppressed, which also explain the noticeable enhancement in electrochemical performance of honeycomb-ordered materials.

4. Conclusions

In summary, we demonstrate an electronic-structure tuning strategy of honeycomb-ordered $Na_3Ni_2SbO_6$ cathode material through the incorporation of Ru cations. Appropriate Ru substitution in the Sb site significantly improves the electronic conductivity, Na^+ diffusion kinetics and structural integrity, leading to an increased capacity, better rate performance and cyclability. We attribute the enhanced performance to the 4d empty orbitals introduced by Ru^{4+} and the strong covalency of active Ru cations with oxygen that facilitates the generation of the electronic holes for the O 2p band and stabilizes the honeycomb layered structure. We anticipate that reasonable cationic substitution with different M-O bond energy in layered oxides, such as V^{5+}, Bi^{5+}, Ru^{4+}, Mo^{4+}, etc., can modulate the cationic ordering in the lattice to enhance the electrochemical kinetics and cycling stability, which offer some inspiration in designing layered cathode candidates for high performance SIBs.

Declaration of Competing Interest

None

Supplementary materials

Supplementary material associated with this article can be found, in the online version, at doi:10.1016/j.actamat.2020.08.015.

References

[1] B. Dunn, H. Kamath, J.M. Tarascon, Electrical energy storage for the grid: a battery of choices, Science 334 (6058) (2011) 928–935.

[2] Z. Ding, C. Zhang, S. Xu, J. Liu, C. Liang, L. Chen, P. Wang, D.G. Ivey, Y. Deng, W. Wei, Stable heteroepitaxial interface of Li-rich layered oxide cathodes with enhanced lithium storage, Energy Storage Mater. 21 (2019) 69–76.

[3] C. Zhang, S. Xu, B. Han, G. Lin, Q. Huang, D.G. Ivey, C. Yang, P. Wang, W. Wei, Towards rational design of high performance Ni-rich layered oxide cathodes: the interplay of borate-doping and excess lithium, J. Power Sources 431 (2019) 40–47.

[4] Q. Huang, J. Liu, S. Xu, P. Wang, D.G. Ivey, B. Huang, W. Wei, Roles of coherent interfaces on electrochemical performance of sodium layered oxide cathodes, Chem. Mater. 30 (14) (2018) 4728–4737.

[5] S. Wei, S. Choudhury, J. Xu, P. Nath, Z. Tu, L.A. Archer, Highly stable sodium batteries enabled by functional ionic polymer membranes, Adv. Mater. 29 (12) (2017) 1605512.

[6] N. Yabuuchi, K. Kubota, M. Dahbi, S. Komaba, Research development on sodium-ion batteries, Chem. Rev. 114 (23) (2014) 11636–11682.

[7] G. Xiong, P. He, Z. Lyu, T. Chen, B. Huang, L. Chen, T.S. Fisher, Bioinspired leaves-on-branchlet hybrid carbon nanostructure for supercapacitors, Nat. Commu. 9 (1) (2018) 790.

[8] N. Yabuuchi, M. Kajiyama, J. Iwatate, H. Nishikawa, S. Hitomi, R. Okuyama, R. Usui, Y. Yamada, S. Komaba, P2-type Nax[Fe$_{1/2}$Mn$_{1/2}$]O$_2$ made from earth--abundant elements for rechargeable Na batteries, Nat. Mater. 11 (2012) 512–517.

[9] M.H. Han, E. Gonzalo, G. Singh, T. Rojo, A comprehensive review of sodium layered oxides: powerful cathodes for Na-ion batteries, Energy Environ. Sci. 8 (1) (2015) 81–102.

[10] Q. Huang, J. Liu, L. Zhang, S. Xu, L. Chen, P. Wang, D.G. Ivey, W. Wei, Tailoring alternating heteroepitaxial nanostructures in Na-ion layered oxide cathodes via an in-situ composition modulation route, Nano Energy 44 (2018) 336–344.

[11] C. Delmas, C. Fouassier, P. Hagenmuller, Structural classification and properties of the layered oxides, Physica B+C 99 (1980) 81–85.

[12] X. Lu, Y. Wang, P. Liu, L. Gu, Y.S. Hu, H. Li, G.P. Demopoulos, L. Chen, Direct imaging of layered O$_3$- and P2-NaxFe$_{1/2}$Mn$_{1/2}$O$_2$ structures at the atomic scale, Phys. Chem. Chem. Phys. 16 (40) (2014) 21946–21952.

[13] H. Guo, Y. Wang, W. Han, Z. Yu, X. Qi, K. Sun, Y.S. Hu, Y. Liu, D. Chen, L. Chen, Na-deficient O3-type cathode material Na-0.8 Ni0.3Co0.2Ti0.5 O-2 for room-temperature sodium-ion batteries, Electrochimica Acta 158 (2015) 258-263.

[14] B.M. de Boisse, J.H. Cheng, D. Carlier, M. Guignard, C.J. Pan, S. Bordere, D. Filimonov, C. Drathen, E. Suard, B.J. Hwang, A. Wattiaux, C. Delmas, O3-NaxMn$_{1/3}$Fe$_{2/3}$O$_2$ as a positive electrode material for Na-ion batteries: structural evolutions and redox mechanisms upon Na+ (de) intercalation, J. Mater. Chem. A 3 (20) (2015) 10976–10989.

[15] H. Yu, S. Guo, Y. Zhu, M. Ishida, H. Zhou, Novel titanium-based O-3-type NaTi$_{0.5}$Ni0.5O$_2$ as a cathode material for sodium ion batteries, Chem. Commun. 50 (4) (2014) 457–459.

[16] M.H. Han, E. Gonzalo, M. Casas-Cabanas, T. Rojo, Structural evolution and electrochemistry of monoclinic NaNiO$_2$ upon the first cycling process, J. Power Sources 258 (2014) 266–271.

[17] D. Yuan, X. Liang, L. Wu, Y. Cao, X. Ai, J. Feng, H Yang, A honeycomb-layered Na$_3$Ni$_2$SbO$_6$: a high-rate and cycle-stable cathode for sodium-ion batteries, Adv. Mater. 26 (36) (2014) 6301–6306.

[18] H. Dai, C. Yang, X. Ou, X. Liang, H. Xue, W. Wang, G. Xu, Unravelling the electrochemical properties and thermal behavior of NaNi$_{2/3}$Sb$_{1/3}$O$_2$ cathode for sodium-ion batteries by in situ X-ray diffraction investigation, Electrochimica Acta 257 (2017) 146–154.

[19] J. Ma, S.H. Bo, L. Wu, Y. Zhu, C.P. Grey, P.G. Khalifah, Ordered and Disordered Polymorphs of Na(Ni$_{2/3}$Sb$_{1/3}$)O$_2$: honeycomb-ordered cathodes for Na-ion batteries, Chem. Mater. 27 (7) (2015) 2387–2399.

[20] J. Liu, L. Yin, L. Wu, J. Bai, S.M. Bak, X. Yu, Y. Zhu, X.Q. Yang, P.G. Khalifah, Quantification of honeycomb number-type stacking faults: application to Na$_3$Ni$_2$BiO$_6$ cathodes for Na-ion batteries, Inorg. Chem. 55 (17) (2016) 8478–8492.

[21] P.F. Wang, H.R. Yao, Y. You, Y.G. Sun, Y.X. Yin, Y.G. Guo, Understanding the structural evolution and Na+ kinetics in honeycomb-ordered O'3-Na$_3$Ni$_2$SbO$_6$ cathodes, Nano Res. 11 (6) (2018) 3258–3271.

[22] P.F. Wang, Y.J. Guo, H. Duan, T.T. Zuo, E. Hu, K. Attenkofer, H. Li, X.S. Zhao, Y.X. Yin, X. Yu, Y.G. Guo, Honeycomb-Ordered Na$_3$Ni$_{1.5}$M$_{0.5}$BiO$_6$ (M = Ni, Cu, Mg, Zn) as high-voltage layered cathodes for sodium-ion batteries, ACS Energy Lett. 2 (12) (2017) 2715–2722.

[23] Y. You, S.O. Kim, A. Manthiram, A honeycomb-layered oxide cathode for sodium-ion batteries with suppressed P3-O1 phase transition, Adv. Energy Mater. 7 (5) (2017) 1601698.

[24] L. Xiao, Z. Ding, C. Chen, Z. Han, P. Wang, Q. Huang, P. Gao, W. Wei, Insight into the structural disorder in honeycomb-ordered sodium layered oxide cathodes, iScience (2020) 100898.

[25] C. Liang, F. Kong, R.C. Longo, C. Zhang, Y. Nie, Y. Zheng, K. Cho, Site-dependent multicomponent doping strategy for Ni-rich LiNi$_{1-2}$yCoyMnyO$_2$ (y=1/12) cathode materials for Li-ion batteries, J. Mater. Chem. A 5 (48) (2017) 25303–25313.

[26] Y. Gao, X. Wang, J. Ma, Z. Wang, L. Chen, Selecting substituent elements for Li-Rich Mn-based cathode materials by density functional theory (DFT) calculations, Chem. Mater. 27 (9) (2015) 3456–3461.

[27] P.F. Wang, M. Weng, Y. Xiao, Z. Hu, Q. Li, M. Li, Y.D. Wang, X. Chen, X. Yang, Y. Wen, Y.X. Yin, X. Yu, Y. Xiao, J. Zheng, L.J. Wan, F. Pan, Y.G. Guo, An ordered Ni6-ring superstructure enables a highly stable sodium oxide cathode, Adv. Mater. 31 (43) (2019) 1903483.

[28] M. Sathiya, A.M. Abakumov, D. Foix, G. Rousse, K. Ramesha, M. Saubanere, M.L. Doublet, H. Vezin, C.P. Laisa, A.S. Prakash, D. Gonbeau, G. VanTendeloo, J.M. Tarascon, Origin of voltage decay in high-capacity layered oxide electrodes, Nat. Mater. 14 (2) (2015) 230–238.

[29] W. Schmidt, R. Berthelot, A.W. Sleight, M.A. Subramanian, Solid solution studies of layered honeycomb-ordered phases O$_3$–Na$_3$M$_2$SbO$_6$ (M=Cu, Mg, Ni, Zn), J. Solid State Chem. 201 (2013) 178–185.

[30] S. Sharifi-Asl, F.A. Soto, A. Nie, Y. Yuan, H. Asayesh-Ardakani, T. Foroozan, V. Yurkiv, B. Song, F. Mashayek, R.F. Klie, K. Amine, J. Lu, P.B. Balbuena, R. Shahbazian-Yassar, Facet-dependent thermal instability in LiCoO$_2$, Nano Lett. 17 (4) (2017) 2165–2171.

[31] J. Gázquez, G. Sánchez-Santolino, N. Biškup, M.A. Roldán, M. Cabero, S.J. Pennycook, M. Varela, Applications of STEM-EELS to complex oxides, Mater. Sci. Semicond. Process. 65 (2017) 49–63.

[32] H. Kurata, E. Lefevre, C. Colliex, R. Brydson, Electron-energy-loss near-edge structures in the oxygen K-edge spectra of transition-metal oxides, Phys. Rev. B Condens Matter. 47 (20) (1993) 13763–13768.

[33] D. Qian, B. Xu, M. Chi, Y.S. Meng, Uncovering the roles of oxygen vacancies in cation migration in lithium excess layered oxides, Phys. Chem. Chem. Phys. 16 (28) (2014) 14665–14668.

[34] J. Zheng, G. Teng, C. Xin, Z. Zhuo, J. Liu, Q. Li, Z. Hu, M. Xu, S. Yan, W. Yang, F. Pan, Role of superexchange interaction on tuning of Ni/Li disordering in layered Li(NixMnyCoz)O$_2$, J. Phys. Chem. Lett. 8 (22) (2017) 5537–5542.

[35] J.C. Knight, P. Nandakumar, W.H. Kan, A. Manthiram, Effect of Ru substitution on the first charge-discharge cycle of lithium-rich layered oxides, J. Mater. Chem. A 3 (5) (2015) 2006–2011.

[36] H. Wang, T.A. Tan, P. Yang, M.O. Lai, L. Lui, High-Rate Performances of the Ru–Doped Spinel LiNi$_{0.5}$Mn$_{1.5}$O$_4$: effects of doping and particle size, J. Phys. Chem. C 115 (13) (2011) 6102–6110.

[37] A.C.W.P. James, J.B. Goodenough, Structure and bonding in lithium ruthenate, Li$_2$RuO$_3$, J. Solid State Chem. 74 (2) (1987) 287–294.

[38] B. Li, H. Yan, J. Ma, P. Yu, D. Xia, W. Huang, W. Chu, Z. Wu, Manipulating the electronic structure of li-rich manganese-based oxide using polyanions: towards better electrochemical performance, Adv. Funct. Mater. 24 (32) (2014) 5112–5118.

[39] R. Xiao, H. Li, L. Chen, Density functional investigation on Li$_2$MnO$_3$, Chem. Mater. 24 (21) (2012) 4242–4251.

[40] H. Yu, Y. Qian, M. Otani, D. Tang, S. Guo, Y. Zhu, H. Zhou, Study of the lithium/nickel ions exchange in the layered LiNi$_{0.42}$Mn$_{0.42}$Co$_{0.16}$O$_2$ cathode material for lithium ion batteries: experimental and first-principles calculations, Energy Environ. Sci. 7 (3) (2014) 1068–1078.

[41] M. Leng, J. Bi, W. Wang, R. Liu, C. Xia, Synthesis and characterization of Ru doped NaNi$_{0.5}$Mn$_{0.3}$Ti$_{0.2}$O$_2$ cathode material with improved electrochemical performance for sodium-ion batteries, Ionics 25 (3) (2019) 1105–1115.

[42] J.M. Lim, D. Kim, Y.G. Lim, M.S. Park, Y.J. Kim, M. Cho, K. Cho, The origins and mechanism of phase transformation in bulk Li$_2$MnO$_3$: first-principles calculations and experimental studies, J. Mater. Chem. A 3 (13) (2015) 7066–7076.

[43] B. Song, M.O. Lai, L. Lu, Influence of Ru substitution on Li-rich 0.55Li$_2$MnO$_3$·0.45LiNi$_{1/3}$Co$_{1/3}$Mn$_{1/3}$O$_2$ cathode for Li-ion batteries, Electrochimica Acta 80 (2012) 187–195.

[44] W.J. Lv, Z. Huang, Y.X. Yin, H.R. Yao, H.L.g Zhu, Y.G. Guo, Strategies to build high-rate cathode materials for Na-ion batteries, Chemnanomat 5 (10) (2019) 1253–1262.

[45] R. Takahashi, J.P.L. H.Wang, Electronic structures and conductivity in peptide nanotubes, J. Phys. Chem. B 111 (30) (2007) 9093–9098.

[46] S.C. Yin, Y.H. Rho, I. Swainson, L.F. Nazar, X-ray/Neutron diffraction and electrochemical studies of lithium De/Re-intercalation in Li1-xCo$_{1/3}$Ni$_{1/3}$Mn$_{1/3}$O$_2$(x=0→1), Chem. Mater. 18 (7) (2006) 1901–1910.

[47] J. Xu, Z. Han, K. Jiang, P. Bai, Y. Liang, X. Zhang, P. Wang, S. Guo, H. Zhou, Suppressing cation migration and reducing particle cracks in a layered Fe-based cathode for advanced sodium-ion batteries, Small (2019) 1904388.